

# Polyamine Functionalized Magnetite Nanoparticles as Novel Adsorbents for Cu(II) Removal from Aqueous Solutions

Daniela Cristina Culita<sup>1</sup> · Claudia Maria Simonescu<sup>2</sup> · Rodica Elena Patescu<sup>2</sup> · Silviu Preda<sup>1</sup> · Nicolae Stanica<sup>1</sup> · Cornel Munteanu<sup>1</sup> · Ovidiu Oprea<sup>2</sup>

Received: 18 October 2016 / Accepted: 21 December 2016 / Published online: 7 January 2017  
© Springer Science+Business Media New York 2017

**Abstract** Three novel magnetic adsorbents were synthesized through the immobilization of di-, tri-, and tetraamine onto the surface of silica coated magnetite nanoparticles. The adsorbents were characterized by XRD patterns, FTIR spectroscopy, elemental and thermogravimetric analysis, magnetic measurements, SEM/TEM, EDX spectroscopy, and N<sub>2</sub> adsorption/desorption isotherms. Their capacity to remove copper ions from aqueous solutions was investigated and discussed comparatively. The equilibrium data were analyzed using Langmuir and Freundlich isotherms. The kinetics was evaluated using the pseudo-first-order, pseudo-second-order, and intra-particle diffusion models. The best interpretation for the equilibrium data was given by the Langmuir isotherm for the tri- and tetraamine functionalized adsorbents, while for the diamine functionalized adsorbent the Freundlich model seemed to be better. The kinetic data were well fitted to the pseudo-second-order model. The overall rate of adsorption was significantly influenced by external mass transfer and intraparticle diffusion. It was observed that the adsorption capacity at room temperature decreased as the length of polyamine chain immobilized on the adsorbent surface increased, the maximum adsorption capacities being 52.3 mg g<sup>-1</sup> for 1,3-diaminopropan functionalized adsorbent, 44.2 mg g<sup>-1</sup> for diethylenetriamine functionalized adsorbent, and 39.2 mg g<sup>-1</sup> for triethylenetetramine

functionalized adsorbent. The sorption process proved to be highly dependent of pH. The results of the present work recommend these materials as potential candidates for copper removal from aqueous solutions.

**Keywords** Polyamine functionalized magnetite · Adsorption · Heavy metal

## 1 Introduction

Contamination of wastewater by heavy metals is a very serious environmental problem. Therefore the removal of heavy metals from industrial effluents and wastewater is of major importance. The metals of major concern are lead, mercury, cadmium, chromium, arsenic, copper, aluminium, nickel, zinc [1]. Among them, copper is the most prevalent one, as it is used in many industries such as mining, electroplating, automotive, tanning, textile manufacturing, fertilizer manufacturing, and even food production. Although in trace amounts copper is essential for human health, excess amounts can cause severe health disorders, like nausea, gastrointestinal distress, anorexia, allergies, depression and many others [2]. It is also irritating to the respiratory tract, damages liver and kidney [3].

Current methods for reducing copper include chemical precipitation, reverse osmosis, coagulation, flocculation, membrane filtration, electrochemical treatment, ion exchange [4]. However each of these methods shows certain drawbacks like incomplete removal, high reagents and energy requirements, toxic sludge which may require special treatment and disposal facilities [5]. Among all of treatment processes, the adsorption proved to be a very effective method of removal of even very low levels of heavy metals from their aqueous solutions, because of its

✉ Daniela Cristina Culita  
danaculita@yahoo.co.uk

<sup>1</sup> “Ilie Murgulescu” Institute of Physical Chemistry, 202 Splaiul Independentei, 060021 Bucharest, Romania

<sup>2</sup> Faculty of Applied Chemistry and Materials Science, Politehnica University of Bucharest, 1-7 Polizu Str., 011061 Bucharest, Romania

flexibility in design, simple operation and high efficiency. An ideal adsorbent should have a stable matrix with numerous functional groups suitable for adsorption, high surface area and porosity. Many types of adsorbents have been developed and tested for heavy metal ion removal so far, like carbon-based materials (activated carbon [6], biochar [7], graphite oxide [8], carbon nanotubes [9], functionalized mesoporous silica [10, 11], zeolites [12], bentonite [13], resin [14], clay [15], spinel ferrites [16, 17], magnetic chitosan composites [18], biomasses [19]). In most cases, after adsorption, it is difficult to separate the adsorbents from the aqueous solutions using traditional separation methods such as filtration or sedimentation, because adsorbents may block filters or may be lost. To overcome these problems many recent researches has been focused on the use of magnetic adsorbents as alternative method for treating water/wastewater [20, 21]. The main advantage of this technology is that a large amount of wastewater can be quickly purified using less energy and producing no contaminants [22].

In this study we aimed to synthesize novel magnetic adsorbents through the immobilization of di-, tri-, and tetraamine onto the surface of silica coated magnetite nanoparticles and to investigate comparatively their ability to remove copper ions from aqueous solutions. The synthesized materials were characterized with respect to their structural, morphological, compositional, and magnetic properties. The influence of the different types of amine groups and the steric factors affecting the adsorption process have been investigated in detail. Copper uptake was quantitatively evaluated using the Langmuir and Freundlich models. Kinetic data were evaluated by the pseudo-first order, pseudo-second order, and intraparticle diffusion model.

## 2 Experimental

### 2.1 Materials

Ferric chloride hexahydrate ( $\text{FeCl}_3 \cdot 6\text{H}_2\text{O}$ ), ferrous chloride tetrahydrate ( $\text{FeCl}_2 \cdot 4\text{H}_2\text{O}$ ) were purchased from Fluka. 3-(Chloropropyl)-trimethoxysilane (CIPTS), diethylenetriamine (DETA), triethylenetetramine (TETA), 1,3-diaminopropane (DAMP), copper nitrate trihydrate ( $\text{Cu}(\text{NO}_3)_2 \cdot 3\text{H}_2\text{O}$ ), hydrochloric acid 37%, acetonitrile, triethylamine were purchased from Merck. Ammonia solution 25% ( $\text{NH}_4\text{OH}$ ) and ethanol absolute were provided by Chimreactiv. All chemicals were used in the received state without any further purification. Deionized water was used in the experiments.

### 2.2 Synthesis of $\text{Fe}_3\text{O}_4$ @CIPTS

The magnetite nanoparticles were prepared by a chemical coprecipitation method, according to a previously reported procedure [23]. The as-prepared magnetite (3.7 mmol) were dispersed in 50 mL water/ethanol (volume ratio 1:4) acidified with few drops of HCl 37%, by ultrasonication, then 2.6 mL 3-(chloropropyl)-trimethoxysilane were added to this suspension and ultrasonicated for another 15 min. The resulted mixture was kept at 45 °C under continuous stirring for 48 h. At the end of this process, the resulting solid was collected using a permanent magnet, washed several times with ethanol and then dried in oven at 80 °C for 2 h. The material obtained was denoted as  $\text{Fe}_3\text{O}_4$ @CIPTS.

### 2.3 Synthesis of $\text{Fe}_3\text{O}_4$ @DETA, $\text{Fe}_3\text{O}_4$ @TETA, $\text{Fe}_3\text{O}_4$ @DAMP

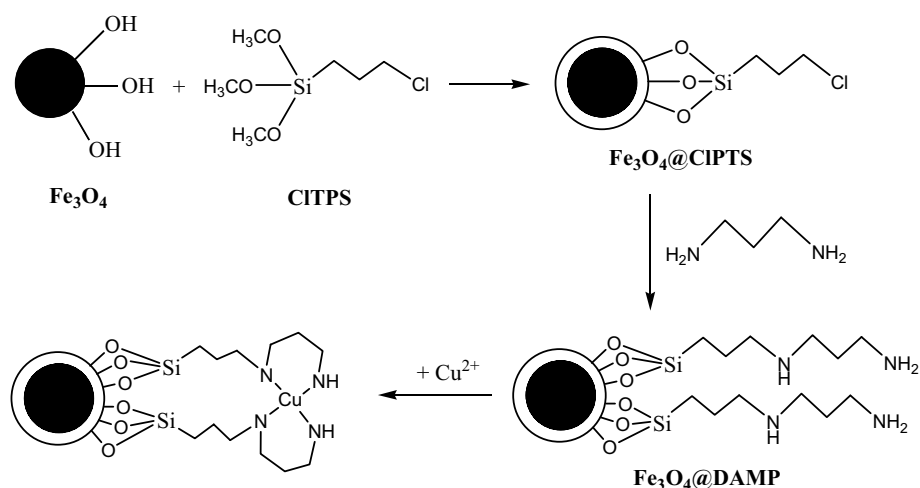
To a suspension of the as-synthesized  $\text{Fe}_3\text{O}_4$ @CIPTS in acetonitrile (80 mL), a slight excess of DETA (2 mL) and 0.5 mL triethylamine were added dropwise and the reaction mixture was stirred for 24 h under reflux. The product was recovered magnetically, washed several times with ethanol and dried at 80 °C for 6 h. The same procedure was applied for the synthesis of  $\text{Fe}_3\text{O}_4$ @TETA,  $\text{Fe}_3\text{O}_4$ @DAMP, but using the appropriate amount of TETA (2.5 mL) and DAMP (1.5 mL).

The experimental process for magnetite functionalization and the subsequent adsorption of Cu(II) ions is illustrated in Scheme 1.

### 2.4 Characterization

Powder X-ray diffraction patterns (XRD) were recorded on a Rigaku Ultima IV apparatus, with  $\text{CuK}_\alpha$   $\lambda = 1.5406 \text{ \AA}$  radiation, in the  $2\theta = 10\text{--}80^\circ$  range, with a speed of  $5^\circ \text{ min}^{-1}$  and a 0.02 steps size, at 40 kV and 30 mA. FTIR spectra were obtained on the substances pressed into KBr pellets in the range 400–4000  $\text{cm}^{-1}$  with Jasco FTIR 4100 spectrophotometer. The content of nitrogen and carbon in samples was determined through elemental analysis on a EuroEA elemental analyzer. The thermal analysis (TG/DSC) of the compounds was performed with a Netzsch TG 449C STA Jupiter. Samples were placed in alumina crucible and heated with  $10^\circ \text{C min}^{-1}$  from room temperature to 900 °C, in air. The magnetization versus magnetic field strength investigations at room temperature, were performed on a Lake Shore's fully integrated Vibrating Sample Magnetometer system 7404. The morphology of the samples were investigated by scanning electron microscopy (SEM) using a high-resolution microscope, FEI Quanta 3D FEG model, at low accelerating voltage (2–5 kV), in

**Scheme 1** Schematic illustration of the chemical process for obtaining the adsorbent  $\text{Fe}_3\text{O}_4@$ DAMP and the subsequent adsorption of  $\text{Cu}(\text{II})$  ions. For the other two adsorbents,  $\text{Fe}_3\text{O}_4@$ DETA and  $\text{Fe}_3\text{O}_4@$ TETA, the synthetic procedure was similar



high vacuum mode with Everhart–Thornley secondary electron (SE) detector and backscatter electron detector. Samples preparation was minimal and consisted in immobilizing the material on a double-sided carbon tape, without coating. Elemental analysis measurements by Energy Dispersive X-ray (EDX) spectroscopy were carried out in the same apparatus, operating at an accelerating voltage of 20 kV. The transmission electron microscopy (TEM) measurements were performed on FEI Tecnai G2 F30 S-Twin microscope at an accelerating voltage of 300 kV. A little amount of sample suspended in ethanol was drop-casted on holey carbon-coated copper grids and subsequently air-dried before TEM analysis. Nitrogen sorption isotherms at  $-196\text{ }^\circ\text{C}$  were recorded on a Micromeritics ASAP 2020 automated gas adsorption system. All the samples were degassed under vacuum prior to  $\text{N}_2$  adsorption at  $90\text{ }^\circ\text{C}$  for 9 h. Specific surface areas ( $S_{\text{BET}}$ ) were calculated according to the Brunauer–Emmett–Teller (BET) equation using adsorption data at  $p/p_0=0.05\text{--}0.30$ , while pore size distributions were derived from the desorption branch using the Barrett–Joyner–Halenda (BJH) model. An AAS 1N Carl Zeiss Jena Atomic Adsorption Spectrophotometer was used to determine copper ions concentration in initial and in solutions after adsorption.

In order to determine the value of point of zero charge ( $\text{pH}_{\text{pzc}}$ ),  $0.01\text{ M}$  NaCl solution was prepared and its initial pH ( $\text{pH}_i$ ) was adjusted between 2 and 10 with  $0.1\text{ N}$  HCl and  $0.01\text{ N}$  NaOH solutions, using a Mettler-Toledo Seven Go Duo pH meter. A given amount of adsorbent ( $0.01\text{ g}$ ) was added to  $10\text{ mL}$  of  $0.01\text{ M}$  NaCl solution and shaken for 24 h on a Heidolph Rotamax 120 platform shaker at  $30\text{ }^\circ\text{C}$ . After this time each resulting pH was measured and the initial pH ( $\text{pH}_i$ ) versus the difference between the initial and final pH values was plotted. The pzc was taken as the point where  $\text{pH}=0$  [24].

## 2.5 Adsorption Experiments

Batch experiments were performed to determine the sorption capacity and factors that influence the adsorption process. A stock solution of  $\text{Cu}(\text{II})$  ( $1000\text{ mg L}^{-1}$ ) was prepared by dissolving an appropriate amount of  $\text{Cu}(\text{NO}_3)_2 \cdot 3\text{H}_2\text{O}$  in distilled water. The working solutions (concentrations ranging from  $5.20$  to  $111.7\text{ mg L}^{-1}$ ) were obtained by stepwise dilution of the stock solution. The initial  $\text{Cu}(\text{II})$  concentrations were determined by atomic absorption spectroscopy (AAS). Typically,  $25\text{ mg}$  adsorbent was dispersed in  $25\text{ mL}$  of aqueous solution containing selected concentrations of  $\text{Cu}(\text{II})$ . The suspensions were shaken in a rotary GFL shaker 3015 ( $150\text{ rpm}$ ) at room temperature, for different time intervals. After adsorption, the adsorbent was removed from solution using a hand-held magnet, the solutions were filtered and the residual concentration of  $\text{Cu}(\text{II})$  was determined by AAS. The following equation was used to calculate the amount of  $\text{Cu}(\text{II})$  adsorbed at equilibrium:

$$Q_e = \frac{(C_i - C_e) \cdot V}{m} \quad (1)$$

where  $Q_e$ —the amount of  $\text{Cu}(\text{II})$  adsorbed at equilibrium ( $\text{mg g}^{-1}$ ),  $C_i$ —the initial concentration of  $\text{Cu}(\text{II})$  solution ( $\text{mg L}^{-1}$ ),  $C_e$ —the equilibrium concentration of  $\text{Cu}(\text{II})$  solution ( $\text{mg L}^{-1}$ ),  $V$ —total volume of  $\text{Cu}(\text{II})$  solution ( $\text{L}$ ) and  $m$ —mass of the adsorbent used ( $\text{g}$ ).

Optimization of adsorption tests was done by studying process parameters such as pH and contact time. The effect of pH was studied in the range from 2 to 6.5, at room temperature. The initial pH of the solutions was adjusted using  $\text{HNO}_3\text{ 1N}$  or  $\text{NaOH 0.1N}$ . The suspensions were shaken for 24 h, then magnetically separated and the residual  $\text{Cu}(\text{II})$  concentration was analyzed. The effect of the contact time between solution and adsorbent was studied in the range of  $5\text{--}600\text{ min}$ , at copper concentration of  $111.7\text{ mg L}^{-1}$ , at

room temperature. The other adsorption parameters were maintained constant.

The equilibrium studies have been accomplished to determine the isotherm model that best describes the adsorption process. The experiments were carried out using Cu(II) solutions with the following concentrations: 5.20, 12.88, 29.26, 54.33, 81.70, and 111.70 mg L<sup>-1</sup>, at optimum pH (above determined) and 24 h contact time.

### 3 Results and Discussion

The immobilization of di-, tri-, and tetraamine functional groups onto the surface of silica coated magnetite nanoparticles was performed by nucleophilic substitution of chloride ion from the 3-chloropropyl-functionalized silica coated magnetite with amine group. The general procedure involved the reaction of 3-chloropropyl-functionalized silica coated magnetite with an excess of the corresponding amine in the presence of triethylamine as a HCl scavenger (Scheme 1).

#### 3.1 Characterization of the Adsorbents

The crystalline structure of the adsorbents was investigated by powder XRD. Figure 1 shows the XRD diffraction patterns in which the six diffraction peaks (220), (311), (400), (422), (511) and (440) characteristic to the spinel structure of magnetite nanoparticles are identified for each adsorbent. No other crystalline phases are detected. The crystallite sizes calculated using the Williamson-Hall method were found to be 6.2 nm for Fe<sub>3</sub>O<sub>4</sub>@DAMP, 8.4 nm for Fe<sub>3</sub>O<sub>4</sub>@DETA, and 8.1 nm for Fe<sub>3</sub>O<sub>4</sub>@TETA respectively.

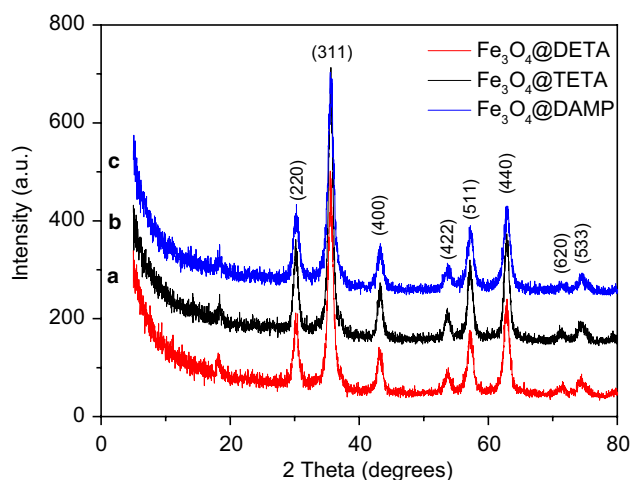


**Fig. 1** XRD patterns of: **a** Fe<sub>3</sub>O<sub>4</sub>@DETA, **b** Fe<sub>3</sub>O<sub>4</sub>@TETA, and **c** Fe<sub>3</sub>O<sub>4</sub>@DAMP

The successful grafting of chloropropylsilane over the magnetite surface and the subsequent reaction with polyamine (DETA, TETA, DAMP) were confirmed by FTIR spectroscopy (Fig. 2). The peak at 1006 cm<sup>-1</sup> which can be attributed to the Si–O–Si asymmetric stretching vibration indicates the formation of silica shell on the surface of Fe<sub>3</sub>O<sub>4</sub>. The peaks at 2937, 2880, and 1475 cm<sup>-1</sup> are typical for asymmetric, symmetric stretching and scissoring vibrations of –CH<sub>2</sub>– group belonging to polyaminic chain [25]. The bands at ~1560 and 1317 cm<sup>-1</sup> present in all amine functionalized samples are related to the N–H stretching and C–N bending vibrations, indicating the successful reaction between chloropropyl and amine groups [26]. The presence of magnetite nanoparticles was confirmed by the strong absorption band at around 580 cm<sup>-1</sup> which corresponds to the Fe–O bond.

Thermogravimetric analysis was used to determine the content of organic functional groups of the samples. Figure 3 shows the TG/DSC curves obtained. For all the samples, including the intermediate Fe<sub>3</sub>O<sub>4</sub>@CIPTS, the small weight loss at temperatures below 140 °C can be associated with water desorption from the surface of the silica layer. The weight loss from 140 to 440 °C (6.28% for Fe<sub>3</sub>O<sub>4</sub>@DAMP, 7.13% for Fe<sub>3</sub>O<sub>4</sub>@DETA, 6.84% for Fe<sub>3</sub>O<sub>4</sub>@TETA) results from the decomposition of organic phase grafted to the silica surface. As can be seen in Fig. 3, the decomposition of the organic phase occurs in two stages, each of them being accompanied by a relatively intense exothermic peak on the DSC curve. The decomposition process of the organic phase is different in the case of Fe<sub>3</sub>O<sub>4</sub>@CIPTS for which only one step can be observed with an exothermic effect on DSC curve. The last decomposition stage occurring in the range 440–900 °C,

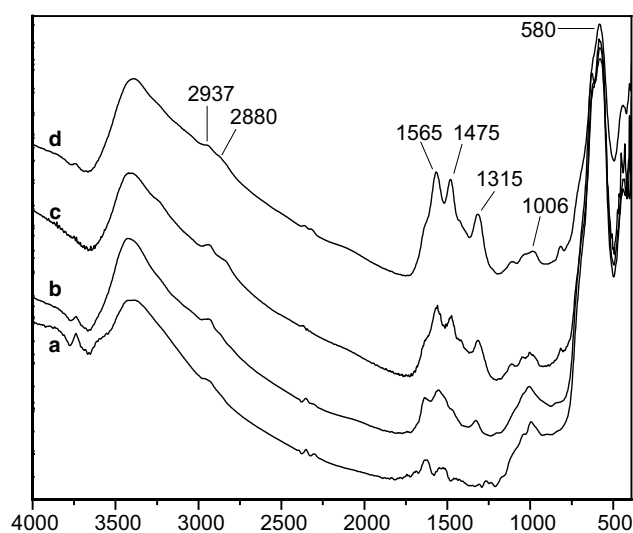


**Fig. 2** FTIR spectra of: **a** Fe<sub>3</sub>O<sub>4</sub>@CIPTS, **b** Fe<sub>3</sub>O<sub>4</sub>@DAMP, **c** Fe<sub>3</sub>O<sub>4</sub>@TETA, **d** Fe<sub>3</sub>O<sub>4</sub>@DETA

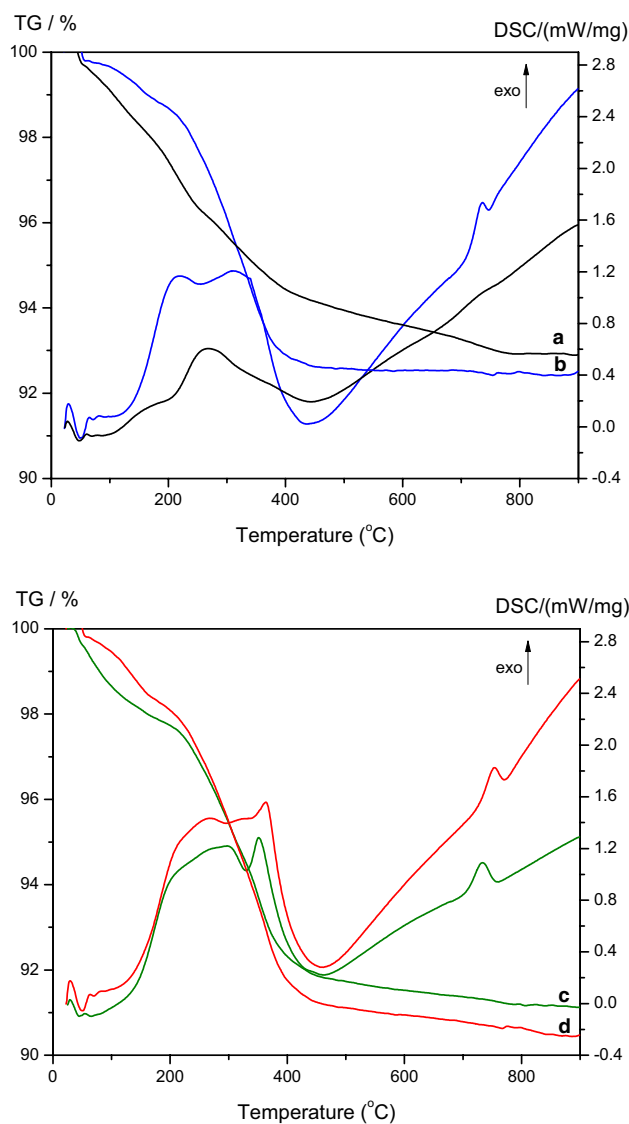


**Fig. 3** Thermal decomposition curves of the samples: **a**  $\text{Fe}_3\text{O}_4$ @CIPTS; **b**  $\text{Fe}_3\text{O}_4$ @TETA; **c**  $\text{Fe}_3\text{O}_4$ @DAMP; **d**  $\text{Fe}_3\text{O}_4$ @DETA

accompanied by a very small weight loss could be attributed to the dehydroxylation of silica network and oxidation of magnetite to maghemite.

The amount of di-, tri-, and tetraamine grafted on the surface of magnetite was also evaluated using C and N elemental analysis as presented in Table 1. The loaded N per gram of  $\text{Fe}_3\text{O}_4$ @DAMP,  $\text{Fe}_3\text{O}_4$ @DETA,  $\text{Fe}_3\text{O}_4$ @

TETA was estimated to be 0.97, 1.38 and 1.35 mmol N  $\text{g}^{-1}$  respectively. These values are in good agreement with those determined on the basis of thermal analysis.

The magnetic properties of the adsorbents were investigated by VSM analysis. The room temperature magnetization versus applied field curves are shown in Fig. 4. All three samples present superparamagnetic behavior since the magnetization curves showed no hysteresis, remanence and coercivity. The saturation magnetization ( $M_s$ ) values were found to be 61.7  $\text{emu g}^{-1}$  for  $\text{Fe}_3\text{O}_4$ @DAMP, 54.7  $\text{emu g}^{-1}$  for  $\text{Fe}_3\text{O}_4$ @DETA, and 57.5  $\text{emu g}^{-1}$  for  $\text{Fe}_3\text{O}_4$ @TETA respectively. These high values suggest the suitability of these nanoadsorbents for magnetic separation. The slight decrease of  $M_s$  values compared to the bulk magnetite (94  $\text{emu g}^{-1}$ ) confirms the presence of the diamagnetic thin layer of silica functionalized with polyamine on the surface of  $\text{Fe}_3\text{O}_4$ .

The morphology of the particles were investigated by scanning electron microscopy (SEM). It can be seen from Fig. 5a–c that all three adsorbents have the same morphology, exhibiting spherical nanoparticles, relatively uniform in size. The mean particle sizes of all the samples are in the nanometric range. Elemental analysis by EDX spectroscopy detected the presence of N in all three samples, besides Fe, Si, O, and C (Fig. 5a–c). The absence of Cl and the appearance of N confirmed the successful reaction between 3-chloropropyl-functionalized silica coated magnetite and polyamines. In order to obtain informations about the particle size distribution, TEM analysis was performed. For exemplification in Fig. 6 is represented a TEM image of  $\text{Fe}_3\text{O}_4$ @DAMP. It can be observed a narrow size distribution of the nanoparticles within the range 5–10 nm. This observation is in very good agreement with the XRD results which indicated that the mean crystallite sizes are smaller than 10 nm.

In order to determine the textural properties of the three prepared adsorbents, the nitrogen adsorption/desorption method was employed. The adsorption–desorption isotherms and the corresponding pore size distribution (PSD) curves are shown in Fig. 7. It can be seen that all isotherms are type IV accompanied by H3 hysteresis loop, according to the IUPAC classification [27], characteristic for mesoporous structures. This type of hysteresis loop could be associated with the presence of slit shape pores in the analyzed materials. It is worth noting that the surface area

**Table 1** Textural and magnetic properties of the samples and the results of elemental analysis

Sample	$S_{\text{BET}}$ ( $\text{m}^2 \text{g}^{-1}$ )	$M_s$ ( $\text{emu g}^{-1}$ )	Elemental analysis (%)			
			C	H	N	C/N
$\text{Fe}_3\text{O}_4$ @DAMP	138.6	61.7	4.31	1.24	1.36	3.16
$\text{Fe}_3\text{O}_4$ @DETA	113.5	54.7	4.68	1.11	1.94	2.41
$\text{Fe}_3\text{O}_4$ @TETA	99.0	57.5	4.33	1.10	1.89	2.29

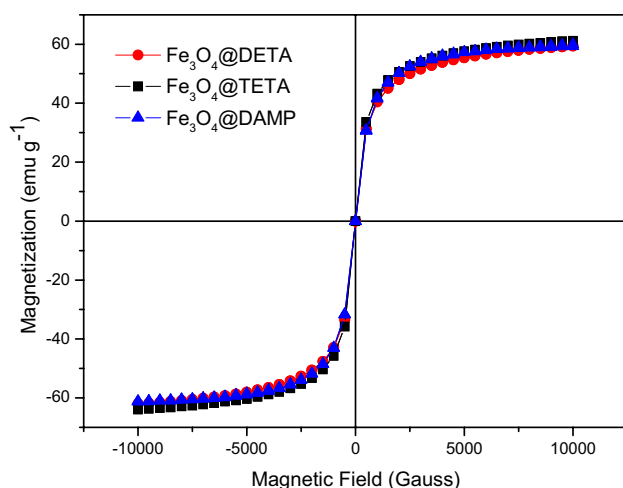


**Fig. 4** Magnetization curves of the samples

of the samples decreases as the number of amine groups in the polyaminic chain increases (Table 1). This trend could be explained by the steric hindrance effects caused by the polyaminic chain length. A longer chain is more likely to obstruct the pores of the silica shell than a short one. It can be observed a monomodal pore size distribution with peaks centered at 6.4 and 8 nm for the samples  $\text{Fe}_3\text{O}_4$ @DAMP and  $\text{Fe}_3\text{O}_4$ @TETA respectively, and a bimodal one for  $\text{Fe}_3\text{O}_4$ @DETA (two peaks centered at 8.9 and 29.6 nm) (Fig. 7b).

## 3.2 Adsorption Studies

### 3.2.1 Equilibrium Adsorption Isotherms

Analysis of equilibrium data provide important informations which help to describe the interaction between an adsorbent and a solute under equilibrium conditions and to evaluate the adsorption capacity of the adsorbent. To understand the adsorption mechanism, the equilibrium data were evaluated according to the Langmuir and Freundlich models (Fig. 8).

The Langmuir model assumes that the adsorption takes place on a limited number of sites characterized by equal adsorption energy, without interactions between sorbed species, indicating monolayer coverage of adsorbate onto a homogeneous adsorbent surface [28]. The Langmuir model is expressed by the following equation:

$$Q_e = \frac{K_L Q_m C_e}{1 + K_L C_e} \quad (2)$$

$C_e$  ( $\text{mg L}^{-1}$ ) is the equilibrium concentration of the adsorbate;  $Q_e$  ( $\text{mg g}^{-1}$ ) is the amount of Cu(II) adsorbed at equilibrium;  $Q_m$  ( $\text{mg g}^{-1}$ ) is the maximum adsorption capacity corresponding to complete monolayer coverage;  $K_L$

( $\text{L mg}^{-1}$ ) is the Langmuir adsorption equilibrium constant related to the adsorption energy.

The Freundlich model assumes that the sorption process occurs on heterogeneous surfaces having various active sites with different binding energies, and sorption capacity is associated with the concentration of adsorbate in the liquid phase at equilibrium [28]. The Freundlich isotherm is expressed as:

$$Q_e = K_F \cdot C_e^{1/n} \quad (3)$$

where  $K_F$  and  $n$  are the Freundlich characteristic constants.

The experimental data were plotted according to the above mentioned isotherm models. The parameters of the equilibrium models were obtained by non-linear regression analysis and summarized in Table 2. The goodness of the fittings to the experimental data was confirmed by the determination coefficient ( $R^2$ ), the Akaike's Information Criterion (AIC) and the evidence ratio. Lower AIC values (on a scale from  $-\infty$  to  $+\infty$ ) indicate that the corresponding model is more likely to occur than the alternative models and the evidence ratio is a numerical value that represents the number of times that the model with the lower AIC is more likely to be correct [29].

According to the data presented in Table 2, the Langmuir model seemed to be more reliable to adjust the experimental data for  $\text{Fe}_3\text{O}_4$ @DETA and  $\text{Fe}_3\text{O}_4$ @TETA as confirmed by the higher determination coefficients ( $R^2$ ) and smaller AIC values in comparison with Freundlich model. The calculus of the evidence ratio also indicates that the Langmuir model is 77 ( $\text{Fe}_3\text{O}_4$ @DETA) and 13 times ( $\text{Fe}_3\text{O}_4$ @TETA) respectively, more likely to be correct than the Freundlich model. In the case of  $\text{Fe}_3\text{O}_4$ @DAMP the  $R^2$  and AIC values indicated the Freundlich model being better to adjust the experimental data, the evidence ratio indicating that this model is only 0.24 times more likely to be correct than Langmuir. Maximum adsorption capacities for Cu(II) calculated from the Langmuir equation were: 52.3  $\text{mg g}^{-1}$  for  $\text{Fe}_3\text{O}_4$ @DAMP, 44.2  $\text{mg g}^{-1}$  for  $\text{Fe}_3\text{O}_4$ @DETA, and 39.2  $\text{mg g}^{-1}$  for  $\text{Fe}_3\text{O}_4$ @TETA, respectively. The degree of suitability of these adsorbents towards copper ions was estimated from the values of the separation factor constant ( $R_L$ ), in the following relation:

$$R_L = \frac{1}{1 + K_L C_0} \quad (4)$$

where  $C_0$  ( $\text{mg L}^{-1}$ ) is the initial Cu(II) concentration, and  $K_L$  is the Langmuir equilibrium constant. The  $R_L$  values indicate whether the adsorption is unfavorable ( $R_L > 1$ ), linear ( $R_L = 1$ ), favorable ( $0 < R_L < 1$ ), or irreversible ( $R_L = 0$ ) [30]. The values of  $R_L$  ranging between 0.03 and 0.13 indicate the suitability of the adsorbents for the Cu(II) removal.

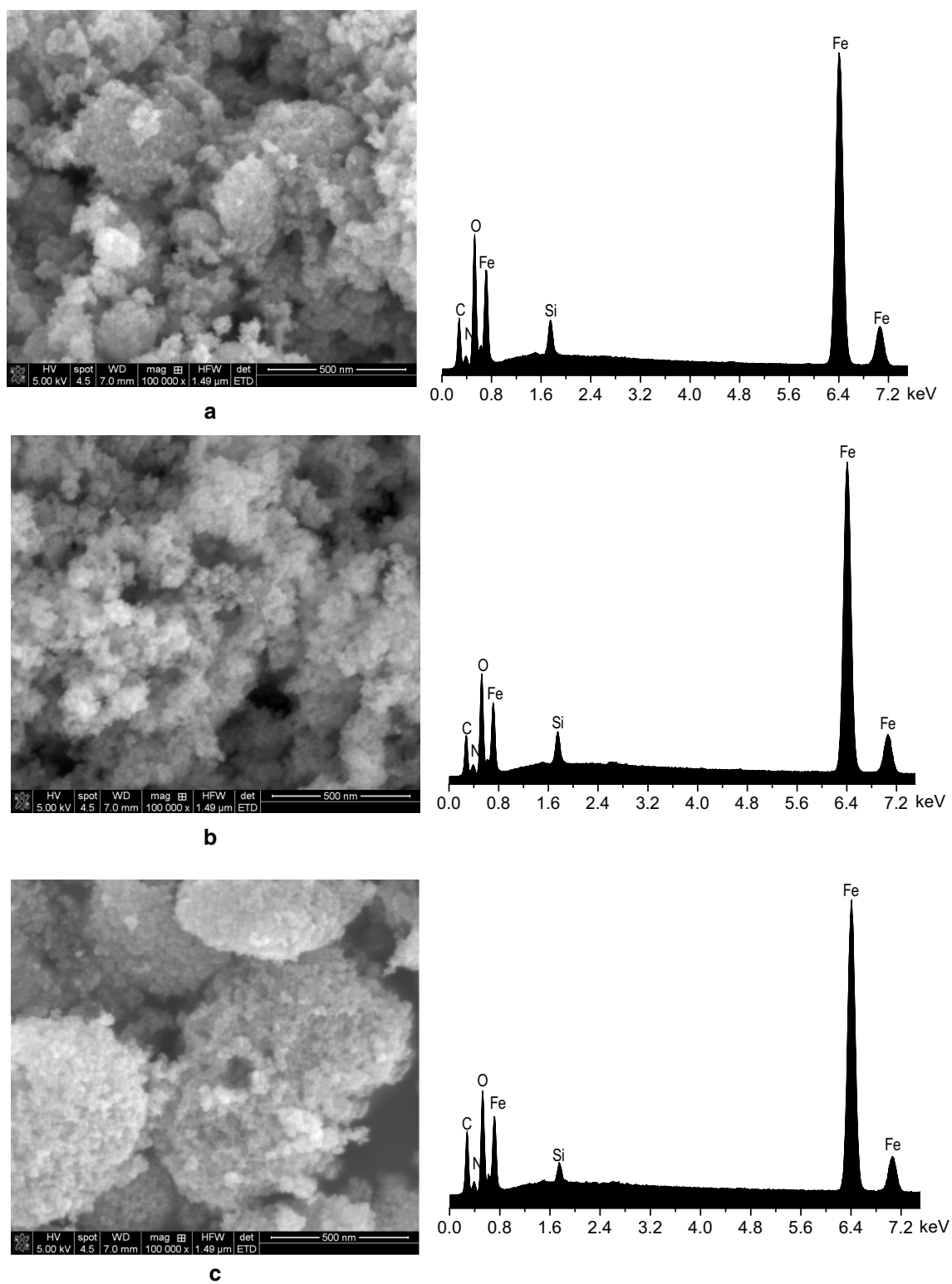


**Fig. 5** SEM micrographs and EDX spectroscopy of the samples  $\text{Fe}_3\text{O}_4$ @DAMP (a),  $\text{Fe}_3\text{O}_4$ @DETA (b), and  $\text{Fe}_3\text{O}_4$ @TETA (c)

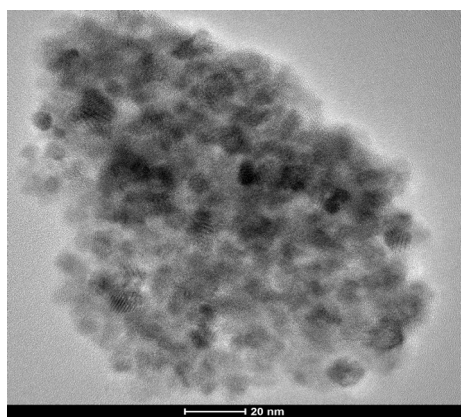


**Fig. 6** TEM image of Fe<sub>3</sub>O<sub>4</sub>@DAMP

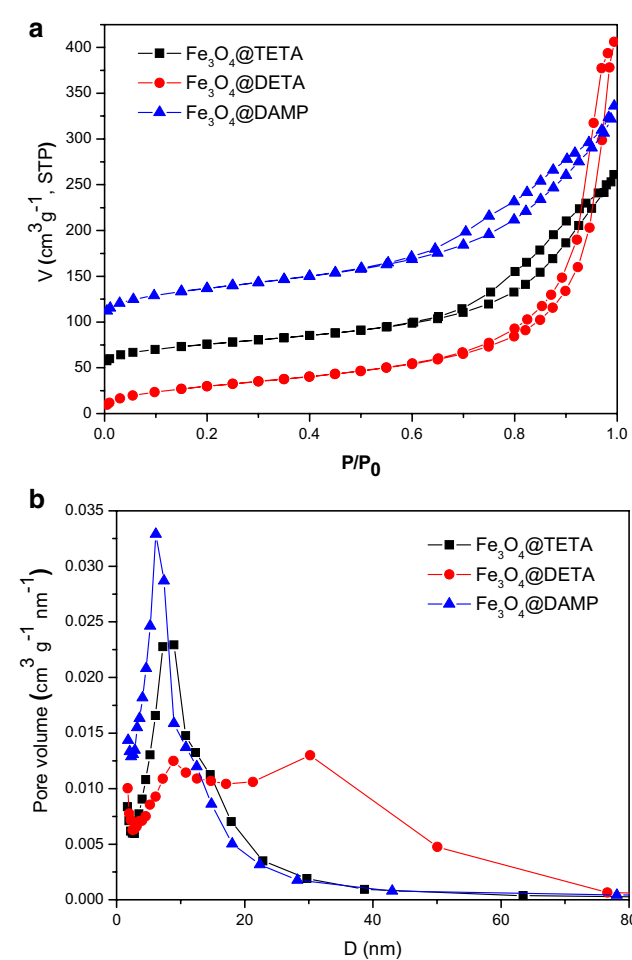
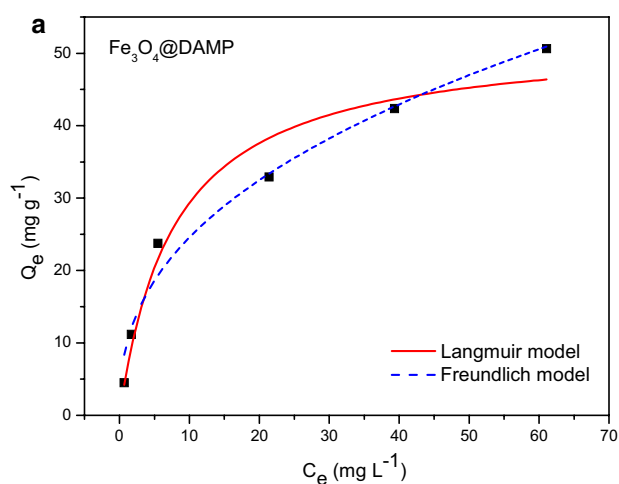


**Fig. 7** N<sub>2</sub> adsorption-desorption isotherms (a) and pore size distribution (b) of the samples. The isotherms of Fe<sub>3</sub>O<sub>4</sub>@TETA and Fe<sub>3</sub>O<sub>4</sub>@DAMP were shifted vertically by 50 and 100 units respectively, for the sake of clarity

In Table 3 are presented the adsorption capacities of various adsorbents for Cu<sup>2+</sup> reported in literature. As can be seen the adsorption capacity of our adsorbents is higher than that of other magnetic adsorbents recently reported.

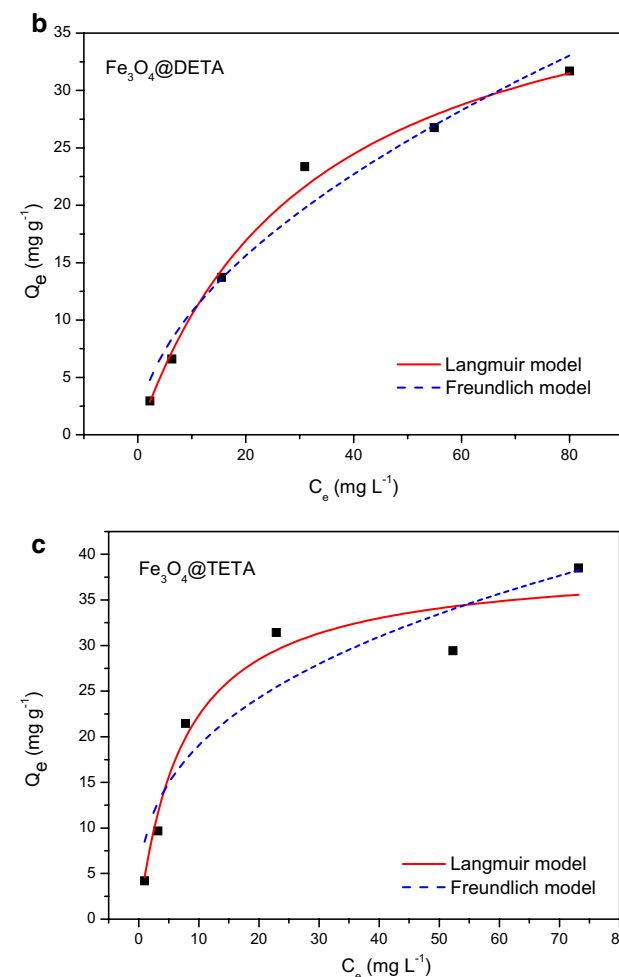


**Fig. 8** Equilibrium adsorption isotherms of Cu(II) on the magnetic adsorbents, at pH=5.5 and 298 K

### 3.2.2 Effect of the Solution pH on Adsorption of Cu(II)

The effect of solution pH on the adsorption of Cu(II) ions by the polyamine functionalized magnetic

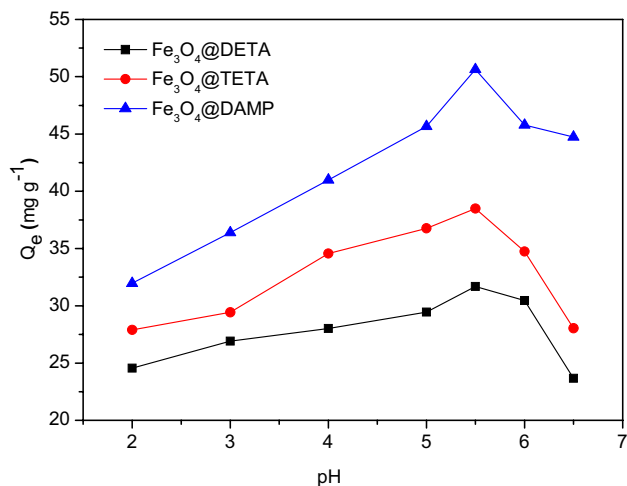


**Table 2** Langmuir and Freundlich isotherm parameters obtained by nonlinear regression

Sample	Langmuir parameters					Freundlich parameters			
	$Q_m$ (mg g <sup>-1</sup> )	$K_L$ (L mg <sup>-1</sup> )	$R^2$	AIC	$R_L$	$K_F$ (mg g <sup>-1</sup> )	n	$R^2$	AIC
Fe <sub>3</sub> O <sub>4</sub> @DAMP	52.3 ± 4.43	0.127 ± 0.041	0.956	31.4	0.127	9.72 ± 1.51	2.48 ± 0.232	0.972	28.6
Fe <sub>3</sub> O <sub>4</sub> @DETA	44.2 ± 3.05	0.031 ± 0.005	0.991	16.9	0.031	3.08 ± 0.84	1.85 ± 0.145	0.960	25.6
Fe <sub>3</sub> O <sub>4</sub> @TETA	39.2 ± 3.33	0.132 ± 0.043	0.939	29.7	0.132	8.49 ± 2.64	2.85 ± 0.120	0.857	34.9

**Table 3** Comparison of adsorption capacity of various adsorbents for Cu<sup>2+</sup>

Adsorbent	Adsorption capacity (mg g <sup>-1</sup> )	Refs.
Magnetic chitosan nanoparticles	35.5	Huang et al. [31]
Amino-functionalized Fe <sub>3</sub> O <sub>4</sub> @SiO <sub>2</sub>	30	Mellah et al. [32]
Fe <sub>3</sub> O <sub>4</sub> /Humic acid	56.3	Wang et al. [33]
Carboxymethyl-cyclodextrin modified Fe <sub>3</sub> O <sub>4</sub>	47.2	Yuan et al. [34]
Gum arabic modified Fe <sub>3</sub> O <sub>4</sub> nanoparticles	38.5	Yuwei et al. [35]
Amino-functionalized polyacrylic acid@Fe <sub>3</sub> O <sub>4</sub>	12.43	Wang et al. [36]
Hyaluronic acid—functionalized magnetic microspheres	29.43	Liu et al. [37]
Amino-functionalized magnetic nanosorbent	25.77	Badruddoza et al. [38]
Fe <sub>3</sub> O <sub>4</sub> @DAMP	52.3	This work
Fe <sub>3</sub> O <sub>4</sub> @DETA	44.2	This work
Fe <sub>3</sub> O <sub>4</sub> @TETA	39.2	This work

**Fig. 9** Effect of the solution pH on the adsorption of magnetic adsorbents towards Cu(II) from aqueous solutions

adsorbents at 25 °C and an initial Cu(II) ion concentration of 111.7 mg L<sup>-1</sup> was shown in Fig. 9. The adsorption experiments were performed in the range of pH from 2 to 6.5. At pH values higher than 6.5, copper ions tend to precipitate as hydroxide species and consequently their uptake cannot be measured precisely.

It was found that the adsorption capacity is highly pH-dependent, increasing with the increase of solution pH

and reaching the maximum at pH 5.5 for all three adsorbents. Because at low solution pH values the amine groups belonging to the adsorbent are protonated, electrostatic repulsive forces between copper ions and adsorbent appear. Furthermore, the high concentration of protons strongly compete with copper ions to interact with the amine groups, decreasing significantly the adsorption of copper ions. By increasing the solution pH, the amine groups tend to transform in their neutral form, thus becoming able to bind copper ions through complexation. At higher pH values, it can be assumed that the amine groups adsorb hydroxyl ions from the solution through hydrogen bonds leading to the formation of  $-NH_2OH^-$  or  $-NH(OH^-)-$  species which are able to electrostatically attract the copper ions [39]. The  $pH_{PZC}$  values of the adsorbents were found to be 8.5 for Fe<sub>3</sub>O<sub>4</sub>@DAMP, 8.6 for Fe<sub>3</sub>O<sub>4</sub>@DETA, and 8.1 for Fe<sub>3</sub>O<sub>4</sub>@TETA. It is worth noting that even at pH values lower than  $pH_{PZC}$ , the adsorbents surface is available for the adsorption of copper ions, this behaviour suggesting the possibility to use these adsorbents for copper ions removal from acidic media.

Comparing the adsorption capacities of the three adsorbents determined from Langmuir equation, it should be noticed that Fe<sub>3</sub>O<sub>4</sub>@DAMP is the highest, followed by Fe<sub>3</sub>O<sub>4</sub>@DETA and Fe<sub>3</sub>O<sub>4</sub>@TETA. Therefore the immobilization of polyamine chains with more amine groups on the adsorbent surface did not favor the adsorption of Cu(II) ions, but on the contrary it hinder it. These results are consistent

with those of other previous studies [25, 26]. This observation is also sustained by the values of specific surface area which follow the same trend. The greater adsorption capacity of  $\text{Fe}_3\text{O}_4\text{@DAMP}$  could be explained by the easiness of the neighboring  $\text{H}_2\text{NCH}_2\text{CH}_2\text{CH}_2\text{NH}-$  groups to form stable complexes with Cu(II) ions (Scheme 1). In case of  $\text{Fe}_3\text{O}_4\text{@DETA}$  and  $\text{Fe}_3\text{O}_4\text{@TETA}$  it is obvious that the longer polyamine chains generates steric hindrance effects leading to less stable Cu(II) complexes and therefore the uptake capacity of the adsorbents is lower.

### 3.2.3 Adsorption Kinetics

The effect of contact time on the sorption process was studied at Cu(II) concentration of  $111.7 \text{ mg L}^{-1}$ , at  $\text{pH}=5.5$ , and the same adsorbent dose ( $25 \text{ mg}/25 \text{ mL}$  solution). As shown in Fig. 10, the amount of Cu(II) ions adsorbed on the three magnetic adsorbents studied increases by increasing the contact time. The main amount of Cu(II) ions ( $\sim 80\%$ ) is adsorbed during the first 60 min due to the high number of amine groups available on the adsorbent surface and to the high solute concentration gradient. After 60 min, the adsorption process starts to become slower due to the gradual decrease of the number of amine groups available for adsorption, and attains equilibrium after 420 min, indicating the saturation of all the adsorption sites.

In order to evaluate the kinetic mechanism that controls the adsorption process, the experimental data were analyzed using two reaction-based models: the pseudo-first-order (Eq. 5) and pseudo-second-order (Eq. 6), and a diffusion-based model, namely intraparticle diffusion (Eq. 7) [31, 40].

$$Q_t = Q_e(1 - e^{-k_1 t}) \quad (5)$$

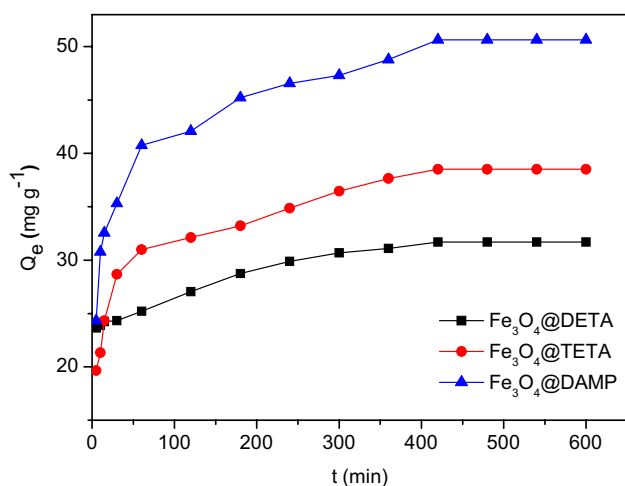


**Fig. 10** Effect of contact time on adsorption of Cu(II) onto magnetic adsorbents

$$Q_t = \frac{Q_e k_2 t}{1 + Q_e k_2 t} \quad (6)$$

$$Q_t = k_{id} t^{0.5} + C \quad (7)$$

where  $Q_e$ ,  $Q_t$  are the amount of Cu(II) adsorbed at equilibrium and at time  $t$  ( $\text{mg g}^{-1}$ ),  $k_1$  is the rate constant of pseudo-first order kinetics ( $\text{min}^{-1}$ ),  $k_2$  is the rate constant of pseudo second-order kinetics ( $\text{g mg}^{-1} \text{min}^{-1}$ ),  $k_{id}$  is the intra-particle diffusion rate constant ( $\text{mg g}^{-1} \text{min}^{-1/2}$ ), and  $C$  is the thickness of the boundary layer ( $\text{mg g}^{-1}$ ).

The parameters of the reaction-based models (pseudo-first-order and pseudo-second-order) were determined by nonlinear regression analysis using GraphPad Prism 7.02 program (trial version). The fittings of the experimental results and the estimated parameters values are presented in Fig. 11 and Table 4.

Comparing the results obtained by fitting the experimental data by the reaction-based models, it was found that the pseudo-second-order model explain better the adsorption kinetic than the pseudo-first-order model in all cases, as evidenced by higher determination coefficients

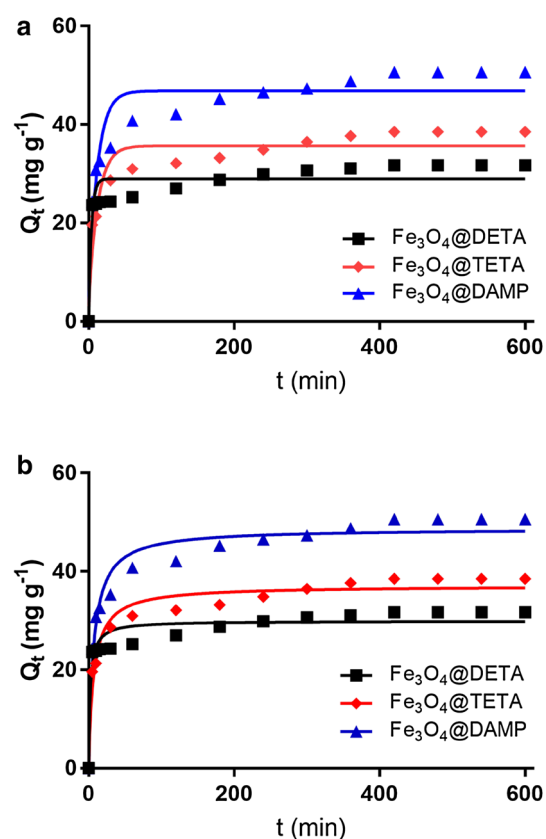


**Fig. 11** Kinetic modelling of the experimental data obtained from the sorption process of Cu(II) onto  $\text{Fe}_3\text{O}_4\text{@DAMP}$ ,  $\text{Fe}_3\text{O}_4\text{@DETA}$  and  $\text{Fe}_3\text{O}_4\text{@TETA}$  using pseudo-first order (a) and pseudo second order (b) models

**Table 4** Kinetic parameters obtained from the fitting of the experimental data with pseudo-first order and pseudo-second order models

Sample	Fe <sub>3</sub> O <sub>4</sub> @DAMP	Fe <sub>3</sub> O <sub>4</sub> @DETA	Fe <sub>3</sub> O <sub>4</sub> @TETA
Q <sub>e</sub> exp (mg g <sup>-1</sup> )	50.6	31.7	38.5
Pseudo-first-order model			
k <sub>1</sub> (min <sup>-1</sup> )	0.084 ± 0.0184	0.255 ± 0.0714	0.0804 ± 0.0176
Q <sub>e</sub> cal (mg g <sup>-1</sup> )	46.8	29.0	35.7
R <sup>2</sup>	0.909	0.877	0.911
AIC	53.8	41.8	45.3
RMSE	4.17	2.80	3.14
Pseudo-second-order model			
k <sub>2</sub> (10 <sup>-3</sup> g mg <sup>-1</sup> min <sup>-1</sup> )	3.03 ± 0.47	14.7 ± 4.38	3.94 ± 0.64
Q <sub>e</sub> cal (mg g <sup>-1</sup> )	48.7	29.9	37.1
R <sup>2</sup>	0.965	0.931	0.962
AIC	35.6	29.3	28.5
RMSE*	2.58	2.10	2.04

\*RMSE root mean square error

(R<sup>2</sup>) and lower AIC and RMSE values. Additionally the Q<sub>e</sub> values obtained from regression (Q<sub>e</sub> cal) using the pseudo-second order model were much closer to the values obtained experimentally (Table 4). This results indicate that the chemisorption is the rate-controlling mechanism [41].

In the case of intraparticle diffusion model a piecewise linear regression was applied to the experimental data using a Microsoft Excel worksheet developed by Malash and El-Khaiary [29]. The results are presented in Fig. 12 and Table 5. According to this model, if the plot is multi-linear or does not pass through the origin, the adsorption process is controlled by two or more diffusion mechanism with different rate constants. If the plot give a straight line which pass through the origin, the adsorption is controlled only by the intraparticle diffusion for the entire adsorption period [42].

For all the three adsorbents the Q<sub>t</sub> versus t<sup>1/2</sup> plots (Fig. 12) indicated the existence of three linear segments which correspond to three operational stages with two breakpoints (the point where two segments meet) representing external mass transfer, intra-particle diffusion and equilibrium of the adsorption process. It can be noticed that the slope of the first segment is not zero, indicating that the adsorption rate is controlled by film diffusion from the beginning until 31–41 min, then changes to intraparticle diffusion control which is maintained until the equilibrium (the second breakpoint, 375–442 min). Therefore, it can be concluded that both mechanisms, film diffusion and intraparticle diffusion are significant for the overall adsorption process.

## 4 Conclusions

Briefly, three novel magnetic nanoadsorbents were prepared through the immobilization of di-, tri-, and tetraamine onto the surface of silica coated magnetite nanoparticles and their sorption capacity for copper ions from aqueous solutions was investigated comparatively. It was observed a decrease of the sorption capacity for copper ions at room temperature with the increasing of polyamine chain length immobilized on the adsorbent surface, this variation being attributed to steric factors. The effect of different parameters like solution pH and contact time on the adsorption process was investigated. The results showed that a pH value of 5.5 is the most favorable for copper adsorption. Almost 80% of total amount of Cu(II) ions was adsorbed during the first 60 min indicating a relatively fast adsorption process. The kinetic studies showed that copper ions adsorption onto all three adsorbents followed a pseudo-second-order kinetics model. The results of intraparticle diffusion model indicated that the adsorption process is significantly influenced by external mass transfer and intraparticle diffusion. The equilibrium adsorption data for Fe<sub>3</sub>O<sub>4</sub>@DETA and Fe<sub>3</sub>O<sub>4</sub>@TETA were well fitted by Langmuir equation, while for Fe<sub>3</sub>O<sub>4</sub>@DAMP the Freundlich model seemed to be better. The maximum adsorption capacities were determined to be 52.3 mg g<sup>-1</sup> for Fe<sub>3</sub>O<sub>4</sub>@DAMP, 44.2 mg g<sup>-1</sup> for Fe<sub>3</sub>O<sub>4</sub>@DETA, and 39.2 mg g<sup>-1</sup> for Fe<sub>3</sub>O<sub>4</sub>@TETA respectively. The obtained results recommend these materials as efficient adsorbents for Cu(II) ions from contaminated water.

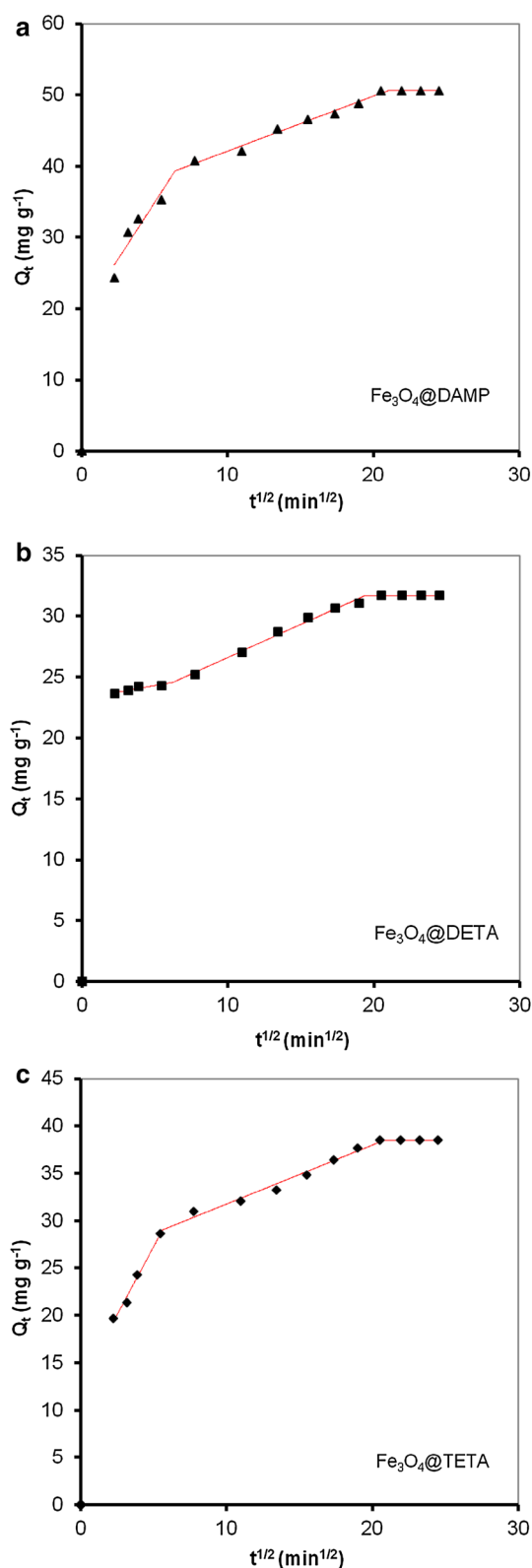


**Fig. 12** Kinetic modelling of the experimental data obtained from the sorption process of Cu(II) onto Fe<sub>3</sub>O<sub>4</sub>@DAMP, Fe<sub>3</sub>O<sub>4</sub>@DETA and Fe<sub>3</sub>O<sub>4</sub>@TETA using the intraparticle diffusion model

**Table 5** Kinetic parameters obtained from the fitting of the experimental data with intraparticle diffusion model

Sample	Break-point (min <sup>1/2</sup> )	k <sub>id</sub> (mg g <sup>-1</sup> min <sup>-1/2</sup> )/ (confidence interval)	C (mg g <sup>-1</sup> )	R <sup>2</sup>
Fe <sub>3</sub> O <sub>4</sub> @DAMP	6.4	3.17/(-0.646 to 6.99)	19.0	0.865
	21.0	0.772/(0.648–0.896)	34.4	0.981
Fe <sub>3</sub> O <sub>4</sub> @DETA	6.2	0.212/(-0.047 to 0.472)	23.2	0.861
	19.4	0.542/(0.452–0.631)	21.2	0.986
Fe <sub>3</sub> O <sub>4</sub> @TETA	5.6	2.87/(1.87–3.87)	12.9	0.987
	20.8	0.623/(0.512–0.735)	25.5	0.976

**Acknowledgements** Financial support of UEFISCDI (Grant PNII—PCCA No. 92/2014) is gratefully acknowledged.

## References

- M. Bilal, J.A. Shah, T. Ashfaq, S.M.H. Gardazi, A.A. Tahir, A. Pervez, H. Haroon, Q. Mahmood, J. Hazard. Mater. **263**, 322–333 (2013)
- X. Xue, F. Li, Micropor. Mesopor. Mat. **116**, 116–122 (2008)
- P. Daraei, S.S. Madaeni, N. Ghaemi, E. Salehi, M.A. Khadivi, R. Moradian, B. Astinchap, J. Membr. Sci. **415–416**, 250–259 (2012)
- A.H. Nguyen, H.H. Ngo, W.S. Guo, J. Zhang, S. Liang, Q.Y. Yue, Q. Li, T.V. Nguyen, Bioresour. Technol. **148**, 574–585 (2013)
- R.N. Ntombani, G.S. Simate, S. Ndlovu, J. Environ. Chem. Eng. **4**, 3143–3150 (2016)
- X. Lu, J. Jiang, K. Sun, G. Zhu, G. Lin, Colloids Surf. A Physicochem. Eng. Asp. **506**, 637–645 (2016)
- S.H. Park, H.J. Cho, C. Ryu, Y.K. Park, J. Ind. Eng. Chem. **36**, 314–319 (2016)
- C. Wang, H. Luo, Z. Zhang, Y. Wu, J. Zhang, S. Chen, J. Hazard. Mater. **268**, 124–131 (2016)
- M.I. Kandah, J.L. Meunier, J. Hazard. Mater. **146**, 283–288 (2007)
- A.M. Liu, K. Hidajat, S. Kawi, D.Y. Zhao, Chem. Commun. **13**, 1145–1146 (2000)
- D.C. Culita, C.M. Simonescu, R.E. Patescu, M. Dragne, N. Stanica, O. Oprea, J. Solid State. Chem. **238**, 311–320 (2016)
- N. Koshy, D.N. Singh, J. Environ. Chem. Eng. **4**, 1460–1472 (2016)
- R.R. Pawar, H.C. Bajaj, S.M. Lee, J. Ind. Eng. Chem. **34**, 213–223 (2016)
- C.K. Liu, R.B. Bai, S.Q. Ly, Water Res **42**, 1511–1522 (2008)
- D. Karamanis, P.A. Assimakopoulos, Water Res **41**, 1897–1906 (2007)
- D. C. Culita, C. M. Simonescu, M. Dragne, N. Stanica, C. Munteanu, S. Preda, O. Oprea, Ceram. Int. **41**(10), 13553–13560 (2015)
- H.K.D. Reddy, Y.S. Yun, Coord. Chem. Rev. **315**, 90–111 (2016)
- D.H.K. Reddy, S.M. Lee, Adv. Colloid Interface Sci **201–202**, 68–93 (2013)
- V.M. Nurchi, I. Villaescusa, Coord. Chem. Rev. **252**, 1178–1188 (2008)

20. L.C.A. Oliveira, D.I. Petkowicz, A. Smaniotto, S.B.C. Pergher, *Water Res.* **38**, 3699–3704 (2004)
21. A.M. El-Toni, M.A. Habila, M.A. Ibrahim, J.P. Labis, Z.A. AlOthman, *Chem. Eng. J.* **251**, 441–451 (2014)
22. Y. Feng, J.L. Gong, G.M. Zeng, Q.Y. Niu, H.Y. Zhang, C.G. Niu, J. Deng, M. Yan, *Chem. Eng. J.* **162**, 487–494 (2010)
23. D.C. Culita, L. Patron, O. Oprea, C. Bartha, P. Palade, V. Teodorescu, G. Filoti, *J. Nanopart. Res.* **15**(9), 1916–1930 (2013)
24. A.M. Cardenas-Peña, J.G. Ibanez, R. Vasquez-Medrano, *Int. J. Electrochem. Sci.* **7**, 6142–6153 (2012)
25. Z.A. Allothman, A.W. Apblett, *J. Hazard. Mater.* **182**, 581–590 (2010)
26. J. Chung, J. Chun, J. Lee, S.H. Lee, Y.J. Lee, S.W. Hong, *J. Hazard. Mater.* **239–240**, 183–191 (2012)
27. K.S.W. Sing, D.H. Everett, R.A.W. Haul, L. Moscou, R.A. Pierotti, J. Rouquerol, T. Siemieniowska, *Pure Appl. Chem.* **57**, 603–619 (1985)
28. S.K. Papageorgiou, F.K. Katsaros, E.P. Kouvelos, J.W. Nolan, H. Le Deit, N.K. Kanellopoulos, *J. Hazard. Mater.* **137**, 1765–1772 (2006)
29. G. F. Malash, M. I. El-Khaiary, *Chem Eng. J.* **163**, 256–263 (2010).
30. X.Y. Huang, J.P. Bin, H.T. Bu, G.B. Jiang, M.H. Zeng, *Carbohydr. Polym.* **84**, 1350–1356 (2011)
31. S.H. Huang, D.H. Chen, *J. Hazard. Mater.* **163**, 174–179 (2009)
32. A. Mellah, S. Chegrouche, M. Barkat, *J. Colloid Interf. Sci.* **296**, 434–441 (2006)
33. T. Wang, X. Jin, Z. Chen, M. Megharaj, R. Naidu, *J. Ind. Eng. Chem.* **20**, 3543–3549 (2014)
34. Q. Yuan, Y. Chi, N. Yu, Y. Zhao, W. Yan, X. Li, B. Dong, *Mater. Res. Bull.* **49**, 279–284 (2014)
35. C. Yuwei, W. Jianlong, *Chem. Eng. J.* **168**, 286–292 (2011)
36. J.H. Wang, S.R. Zheng, Y. Shao, J.L. Liu, Z.Y. Xu, D.Q. Zhu, *J. Colloid Interface Sci.* **349**, 293–299 (2010)
37. J.F. Liu, Z.S. Zhao, G.B. Jiang, *Environ. Sci. Technol.* **42**, 6949–6954 (2008)
38. A.Z.M. Badruddoza, A.S.H. Tay, P.Y. Tan, K. Hidajat, S. M., Uddin, *J. Hazard. Mater.* **185**, 1177–1186 (2011)
39. S.S. Banerjee, D.H. Chen, *J. Hazard. Mater.* **147**, 792–799 (2007)
40. S. Lan, X. Wu, L. Li, M. Li, F. Guo, S. Gan, *Colloids Surf. A* **425**, 42–50 (2013)
41. H. Yong-Mei, C. Man, H. Zhong-Bo, *J. Hazard. Mater.* **184**, 392–399 (2010)
42. B.H. Hameed, M.I. El-Khaiary, *J. Hazard. Mater.* **154**, 237–244 (2008)